Journal of Alloys and Compounds 1066 (2026) 188306

Contents lists available at ScienceDirect

Journal of Alloys and Compounds

journal homepage: www.elsevier.com/locate/jalcom

The origin of anomalous eutectic-like structures in rapidly solidified eutectic Ag-Cu alloys

Huamao Rao *, Robert F. Cochrane, Tiantian Chai, Liam S.E. Teggin, Zabeada Aslam, Stuart Micklethwaite, Andrew M. Mullis

School of Chemical & Process Engineering, University of Leeds, Leeds LS2 9JT, UK

ARTICLE INFO

Keywords:
Rapid solidification
Anomalous eutectic
Solid-state decomposition
Partitionless solidification
Binodal decomposition

ABSTRACT

The formation of anomalous eutectic structures in undercooled eutectic melts has been a subject of enduring interest within the solidification community. In this study, eutectic Ag-Cu alloys were rapidly solidified via drop-tube processing, experiencing cooling rates ranging from 470 to 28000 K s^{-1}, with the corresponding undercooling range being ≈ 20–210 K. Coarse anomalous eutectic structures were observed at eutectic cell margins in all droplets and a fine anomalous eutectic at the cell centres of droplets smaller than 300 μm. A model in which this latter high undercooling anomalous eutectic arises from the growth of a single-phase partitionless solid, followed by binodal phase separation in the solid state appears to provide a consistent explanation for the key observations relating to morphology, chemistry, crystallographic orientation and thermodynamics of the anomalous eutectic and its partitionless precursor. We find either remelting or fragmentation during recalescence are not required under the present conditions.

1. Introduction

When undercooled many binary eutectic alloys display a morphological transition from a regular lamellar structure to one of a range of alternative morphologies [1–10]. These alternate eutectic structures are typically referred to as the *anomalous eutectic*, irrespective of their morphology. Moreover, although much of the literature on the anomalous eutectic is devoted to determining the origin of the morphology, the term itself is a morphological descriptor and does not imply a well-defined mechanistic origin.

The anomalous eutectic is generally coarser than the equilibrium eutectic, typically appearing as coarse blocks or strips [3,4,11], coexisting with the regular eutectic structure. However, in some cases, particularly at high undercooling, the anomalous eutectic can be significantly finer than its regular counterpart. Its volume fraction tends to increase at higher levels of undercooling [4,12], and its spatial distribution is often uneven. The origins of anomalous eutectic formation have been intensively discussed over the past few decades. Proposed models include: coupled [13] or uncoupled growth [7,14] of two phases, remelting of a single dendritic phase [15,16], and remelting or fragmentation mechanisms occurring in the lamellar eutectic [6].

Many authors have proposed a dual mechanism to explain the difference in anomalous eutectics observed under high and low undercooling conditions. In general, it has been suggested that at low undercooling the mechanism tends to be the remelting of either the regular eutectic or eutectic dendrites, whereas at high undercooling this tends to be single-phase dendritic remelting [1,17–19]. Wei et al. [20] found that the anomalous eutectic in Ni-19.6 at% P alloy was fine and uniform below a critical undercooling. However, when the undercooling exceeded 117 K, the distribution of α-Ni phase became very inhomogeneous, with the size difference between coarse and fine particles reaching approximately one order of magnitude. They concluded that the solidification process of the anomalous eutectic formed at high undercooling begins with the α-Ni phase forming as primary supersaturated dendrites from the undercooled melt. These dendrites undergo decomposition due to recalescence. Subsequently, the formation of the β-phase also promotes recalescence. Coupled eutectic growth occurs as the undercooling decreases, while the remelting of the eutectic structure further contributes to the formation of the anomalous eutectic. Yang et al. [18] studied the Ni–Sn eutectic processed via glass fluxing, using the model of Li et al. [1] to calculate the growth competition between eutectic dendrites and dendritic α-Ni. They found that the growth rate of dendritic Ni exceeded that of eutectic dendrities at 160 K, completing the transition from coupled to uncoupled growth. They also observed

* Corresponding author.
E-mail address: ml19h2r@leeds.ac.uk (H. Rao).

https://doi.org/10.1016/j.jallcom.2026.188306
Received 4 January 2026; Received in revised form 23 April 2026; Accepted 27 April 2026
Available online 28 April 2026

that the morphology of the anomalous eutectic under coupled and uncoupled conditions was different in both size and direction.

Similar phenomena have also been reported in other eutectic systems [19–21]. Azadehranjbar et al. [22] studied anomalous eutectics formation in Mg-Al alloys via melt spinning. They identified four types of anomalous eutectics at different wheel speeds. They proposed that at low speeds, anomalous eutectics are generated by remelting of conventional eutectics, typically appearing as standard or spherical eutectic cells. At intermediate speeds, uncoupled growth dominates the formation of anomalous eutectics. In samples solidified at high speeds, the central regions nucleate and are separated by the growth of the eutectic phase. However, at very high speeds, the coupled growth of the eutectic phase is suppressed, leading to the development of a cellular structure.

Wang et al. [23] proposed that the formation of the anomalous eutectic in Ag-Cu under low undercooling resulted from remelting of the lamellar eutectic, also finding that below a critical undercooling, the volume fraction of anomalous eutectic increased with increasing undercooling [12]. Conversely, Mullis et al. [9] studied the Ag Cu alloy system at low undercooling, finding that the volume fraction of the anomalous eutectic far exceeded the volume fraction of solid that could feasibly have formed during the recalescence phase of solidification (in one case ≈50% at an undercooling of just 27 K), which seemingly rules out remelting as a possible mechanism for anomalous eutectic formation. At higher undercooling the morphology of Ag-Cu evolves further with the microstructure transforming into Ag-rich dendrites surrounded by the lamellar eutectic, with it being proposed that upon cooling, the supersaturated solid solution within the dendritic region decomposes into a fine-grained, two-phase mixture [10]. Qin et al. [24] suggested that due to the increase in undercooling, the eutectic point shifts towards more Cu-rich compositions, leading to the formation of primary Ag-rich dendrites, with this model being similar to that employed by Mullis et al. [9].

Numerous studies have demonstrated the breakdown of eutectic growth in the Ag-Cu system at undercoolings of around 70 K [10–12], with coupled eutectic growth giving way to that of single phase, Ag-rich dendrites. Moreover, the Ag-Cu system is unusual in that this critical undercooling for the transition to single phase growth is much closer to the T_0 temperature, the temperature at which the liquid and solid phases of the same composition have the same Gibbs free energy [11,12], than is the case in other eutectic systems, with T_0 for Ag-Cu being reported at around 76 K.

However, at undercoolings significantly in excess of 70 K, it has been proposed that the growth of Cu-rich dendrites will dominate. Zhao et al. [21] used the Boettinger–Coriell–Trivedi (BCT) model [25] to show that the growth rate of β-Cu dendrites is greater than that of α-Ag dendrites, concluding that once the undercooling exceeds ≈ 150 K, β-Cu should be the primary phase. Zhang et al. [26] subsequently observed such Cu dendritic growth in an Ag-50 at%Cu alloy at an undercooling of ≈ 120 K.

During rapid dendritic growth, kinetic solute trapping is commonly observed whereby the partition coefficient k tends towards 1 once the growth velocity V becomes comparable to the velocity characteristic of diffusive solute transport V_D. Models for such solute trapping within the framework of conventional Fickian diffusion, such as those due to Aziz and Kaplan [27,28] predict that for $V >> V_D$, k tends asymptotically towards 1 whereas those constructed within a non-Fickian framework, such as the models of Sobolev [29–32] or Galenko and co-workers [33,34] predicted an abrupt transition to partitionless solidification once V exceeds a critical value. Where anomalous eutectic formation is proposed to occur by the remelting or decomposition of a single phase solid, the non-equilibrium solute concentrations resulting from such kinetic solute trapping may aid such decomposition, irrespective of what type of solute trapping model is assumed.

In addition to kinetic solute trapping, as described above, Baker and Gahn demonstrated that fully partitionless solidification is thermodynamically possible once the temperature at the solid-liquid interface falls below the alloy's characteristic $T0$ temperature [35]. Walder and Ryder [12] came to the similar conclusions, based upon a study of the Ag-Cu system. Eckler et al. [36] used electromagnetic levitation to study deeply undercooled Ni-B alloy, determining the critical undercooling at which crystal growth switches completely to thermal control, associating this with T_0 for the alloy of that composition.

A number of deeply undercooled systems have been postulated to undergo partitionless solidification upon cooling below T_0. Ojha [37] observed a range of phases, including α′ and β in isolated micron size droplets of Cu-12 at% Ag, with β-dendrites surrounded by a featureless interdendritic matrix which they identify as the partitionless solid with composition Cu-28 at% Ag. However, the mechanism they invoke for formation of this partitionless solid appears to ignore this interdendritic liquid being the heat sink for the latent heat released during recalescence, as the temperature of the interdendritic liquid would need to remain constant as it becomes enriched in Ag during β-phase growth. Gusakov et al. [38] observed the distribution of dispersed phases after rapid quenching of Sn-Bi alloys. They observed that at a cooling rate of 10^5 K s^{-1}, a supersaturated solid solution of Bi in Sn was formed by partitionless solidification, with phase decomposition being initiated during quenching. In addition, they observed that the structure formed in Sn–Bi alloys immediately after quenching was consistent with a lamellar eutectic morphology. However, they demonstrated through EBSD analysis that the formation of this structure originated from solid-state decomposition rather than eutectic solidification. Solid-state decomposition was also observed in some high-entropy alloys during the initial solidification stage [39–41]. Teggin et al. [42] used drop-tube processing to prepare $CoCrCuFeNi_{0.8}$ High Entropy Alloy finding nanoscale Cu-rich inclusions dispersed throughout the CoCrCuFe-rich dendrites. They suggest that partitionless solidification of thermally controlled dendrites followed by spinodal decomposition could give the observed structure of Cu-rich dispersion with diameter < 100 nm in a matrix of HEA dendrites. Subsequently, Teggin et al. [42] also observed such dispersions with diameters > 300 nm, which they suggest may originate from binodal decomposition of such a partitionless solid.

In this paper, we revisit the formation of anomalous eutectic structures in the widely studied Ag–Cu eutectic system. An alloy of eutectic composition was processed using a drop-tube apparatus to achieve rapid solidification. Previous studies using this apparatus indicate that droplets typically range in size from slightly less than 1 mm to approximately 38 μm, corresponding to cooling rates spanning roughly two orders of magnitude. The aim of this work is to examine the formation of anomalous eutectic structures across this droplet size range and to clarify the mechanisms responsible for their development.

2. Experimental methods

2.1. Sample preparation and microstructural analysis

A commercial eutectic alloy of nominal composition Ag-39.9 at% Cu was used as the raw material for the drop-tube experiment. The starting ingot, of about 7.5 g, is rapidly solidified via drop-tube processing. The drop-tube operates with a high purity inert atmosphere at a pressure of 40 kPa, with multiple pump/flush cycles being performed prior to processing to ensure an oxygen free environment for droplet solidification. Following melting, during which an approximate 50 K superheat is applied to the melt, the ceramic crucible containing the melt is pressurised to 0.4 MPa, wherein the melt is ejected through three 300 μm holes laser-drilled in the base of the crucible. Solidification of the droplets occurs containerlessly during free-fall, with the resulting powder being collected at the bottom of the tube. A detailed description of the construction and operation of the drop-tube at the University of Leeds has been described previously in the literature [43].

Following cooling, the droplets were collected and sieved into 10 size fractions, namely: > 850 μm, 850–500 μm, 500–300 μm, 300–212 μm, 212–150 μm, 150–106 μm, 106–75 μm, 75–53 μm, 53–38 μm and < 38

μm. Subsequent to droplet collection the powders were mounted using Buehler EpoThin™ 2 epoxy resin and then ground and polished for microscopic analysis. Grinding was performed sequentially using P400, P600, P1200 and P2500 SiC paper. Following grinding, 3 μm and 1 μm diamond paste were used to polish the samples. To achieve a scratch-free surface on the soft eutectic droplets a final polishing step using 0.05 μm colloidal silica was employed. The surface of the samples was cleaned with running water and isopropanol between polishing stages and inspected using optical microscopy to ensure a suitable surface finish.

Following mounting and polishing the samples were carbon coated for SEM analysis, performed using either a Hitachi TM3030Plus SEM (scanning electron microscope) or Hitachi SU8230 SEM operating at 15/20 kV, both equipped with EDX (energy dispersive X-ray) analyzers. Further examination of the samples was performed on selected areas using an FEI Titan^3 Themis 300 TEM (transmission electron microscope) operated in STEM (Scanning Transmission Electron Microscopy) mode at 300 kV to obtain HAADF (high-angle annular dark-field) images. TEM sample preparation was performed using an FEI Helios G4 CX DualBeam FIB (focused ion beam), with the thickness of the resulting FIB cross-section being approximately 90–100 nm.

The 4D-STEM experiments were conducted using a TESCAN Tensor STEM at 100 kV and equipped with a pixelated STEM detector [44]. A convergent electron probe was raster-scanned across the specimen, and a full diffraction pattern was recorded at each probe position, generating a four-dimensional dataset (two-dimensional space × two-dimensional diffraction) that contains both real-space and reciprocal-space information [44]. The accelerating voltage and probe current used in this study were 100 kV and 266 pA, respectively. Since 4D-STEM analysis is based on existing *.cif files (which define the crystallographic lattice parameters), it is necessary to modify these files when dealing with continuous solid-solution phases. Unlike conventional metallic phases, continuous solid solutions exhibit significant compositional variability, which can strongly affect their lattice structure. Therefore, the corresponding lattice parameters in the *.cif files were manually adjusted. For the Ag–Cu system, previous studies have reported that the variation in lattice parameters closely follows Vegard's law, with a deviation of only 1–2% [45]. Based on this relationship, the lattice parameters of Ag and Cu were adjusted according to the compositions measured by TEM–EDX in Fig. 6, the adjusted parameters are summarized in supplementary document.

2.2. Calculation of undercooling and cooling rate of droplets

Based on the balance of heat fluxes, combined with classical nucleation theory, Lee et al. [46] provided a model to estimate the mean undercooling of droplets solidifying in free-fall, as a function of droplet diameter, as shown in Eq. (1). The wetting angle factor $f(\theta)$, which varies with droplet size, was derived by Wang et al. [23] and is shown in Eq. (2), where T_N is the nucleation temperature. Again, further details are provided in the supplementary information supplied with this manuscript. For both equations parameters suitable for a nitrogen environment are provided by [47,48] and are reproduced in the Supplementary Information.

$$\frac{\Psi(\theta)}{(T_N \cdot \Delta T^2)} = \ln\Phi(T_N, \quad \theta, \quad d) \tag{1}$$

$$f(\theta) = \quad -0.0307 \quad + \quad \frac{35.5212}{d} \tag{2}$$

The estimation of undercooling using Eqs. (1) and (2) is subject to significant uncertainty, particularly in the value of K_V. To reduce this uncertainty, the method is calibrated against a microstructural feature that occurs only at a well-defined undercooling. In this system, eutectic growth breaks down in favour of single-phase Ag-rich dendrite growth once the undercooling exceeds approximately 70 K. Consequently, in analysing the as-solidified microstructures we pay particular attention to identifying the largest size fraction in which the formation of single-phase Ag-rich regions are observed. This gives a reliable indication that at least some droplets in that size fraction have attained an undercooling > 70 K, while none of those in any larger size fraction have done so. This in turn constrains the parameter space over which our sensitivity analysis is conducted.

Since the drop-tube experiment simultaneously ejects thousands of droplets that solidify near instantly, it is not possible to determine the thermal history of individual droplets. Therefore, we introduce two heat balance models to calculate the cooling rate and undercooling of the supercooled melt.

The cooling rate for isolated droplets in free-fall can be estimated by calculation of the heat transfer to the surrounding gas at ambient temperature [49,50]. The heat balance may be expressed as:

$$\frac{dT}{dt}[C_p^l(1-f) + C_p^s f] + L\frac{df}{dt} = \frac{6}{d\rho_l}[\varepsilon\sigma_{SB}(T^4 - T_R^4) + (h_m(T - T_R)] \tag{3}$$

Where d is the droplet diameter, C_p^l is the specific heat of the melt, C_p^s the specific heat of the solid, f is the solid fraction, L the latent heat, ρ_l the density of the melt, ε the surface emissivity of the melt, σ_{SB} is the Stefan–Boltzmann constant, T the instantaneous temperature of the droplet, T_R the temperature of the gas (room temperature) and h_m is the heat transfer coefficient of the droplet falling through the gas. Eq. (3) is solved using an explicit Euler time-stepping method, with the droplet temperature and solid fraction being determined at each time-step. More details of this calculation and the values of parameters are given in the Supplementary Information.

2.3. Nucleation time and growth rate calculation

To help estimate the initial phase formed we introduced a model for the competition between nucleation sites that permits an assessment of the nucleation incubation time prior to the onset of growth. Following [51] we write:

$$\tau = \frac{7.2Rf_n(\theta)}{1-\cos\theta} \bullet \frac{a^4}{x_{L,eff} d_a^2} \bullet \frac{T_r}{DS_m \Delta T_r^2} \tag{4}$$

Where $f_n(\theta) = 0.25(2 + \cos\theta)(1 - \cos\theta)^2$, θ is the wetting angle between the solid and liquid phases, a is atomic jump distance, $x_{L,eff} = \frac{x_{L,A}}{x_{S,A}} or \frac{x_{L,B}}{x_{S,B}}$ is the effective alloy concentration, $T_r = \frac{T}{T_M}$, T_M is the melting point of the solid phase, $\Delta T_r = 1 - T_r$, S_m is the molar entropy of fusion and d_a is the atomic radius in the crystalline solid. Typical values for these parameters for the Ag-Cu system are provided by [26,47] and are given in the supplementary information.

We use the Lipton–Kurz–Trivedi (LKT) and Li–Zhang (LZ) models to simulate the relationship between growth rate and undercooling of Ag and Cu dendrites and the Ag-Cu eutectic respectively. To calculate the growth rate for single phase dendrites we use the high Peclet number model originally proposed by Lipton et al. [52]. This is based upon the principle of resolving the total undercooling, ΔT, into its thermal, ΔT_t, constitutional, ΔT_c, curvature, ΔT_r, and kinetic, ΔT_k, contributions, such that:

$$\Delta T = \Delta T_t + \Delta T_c + \Delta T_r + \Delta T_k \tag{5}$$

Specific formulas for these four different undercooling are given by [52], with more details of the calculation provided in the supplementary information.

Li et al. [53] refined the eutectic growth models due to Jackson and Hunt (JH) [54] and Trivedi–Magnin–Kurz (TMK) [55] to better capture the problem of decreased eutectic growth rate and increased lamellar spacing caused by kinetic effects. We therefore use the LZ model to simulate the growth rate of eutectic under higher undercooling, this being:

$$\Delta T = \Delta T_I + \Delta T_t = m\frac{a^L}{\lambda}\left[1+\frac{P}{P+\lambda(\partial P/\partial\lambda)}+\frac{1}{\mu Q^L\lambda}\right]+\frac{\Delta H_f}{C_P}Iv(P_t) \quad (6)$$

Where ΔT_I is undercooling at the interface, ΔT_t is thermal undercooling, and a^L, a^L, m, Q^L are as given in [53], with more details of the calculation being provided in the Supplementary Information.

3. Results

3.1. Microstructure analysis and inner anomalous eutectic occurrence

Fig. 1 shows SEM backscattered electron (BSE) images from four different droplets size ranges. In the 850–300 μm range (Fig. 1a & 1b), the major obtained microstructure showed a mixture of regular lamellar eutectic and the coarse anomalous eutectic. The anomalous eutectic structure appeared at the edge of the eutectic cells, with the volume fraction of anomalous material tending to increase with increasing undercooling (decreasing droplet size), consistent with previous reports [9,10]. As shown in Fig. 1c, for droplets in the 300–212 μm size range, single-phase Ag-rich regions start to appear with these proto-dendrites surrounded by the regular eutectic which radiates outwards from these single-phase regions. The breakdown of eutectic growth in the Ag-Cu system in favour of single-phase Ag growth is well documented in the literature, with the critical undercooling for this being at around 70 K [9,24]. Conversely, Fig. 1d also shows a droplet from the 300–212 μm sieve fraction but is devoid of single-phase Ag-rich regions. Instead, we now observe a second distinct anomalous eutectic morphology, now located at the centre of the eutectic cells. This second anomalous eutectic morphology comprises isolated Cu-rich regions embedded within an Ag-rich matrix and is significantly finer than that of either the regular eutectic, or of the anomalous eutectic located at the cell margins. This morphology is consistent with the report of and Zhao et al. [56]. However, as shown in Fig. 1e and f, in the smallest droplets we rarely observed single-phase Ag-rich regions, with most of the cell centres occupied by this fine anomalous eutectic morphology. Moreover, in droplets < 300 μm in diameter we also tend to observe small Cu-rich dendritic fragments at the eutectic cell margins, with this being most apparent in Fig. 1e which is for a droplet from the 212–150 μm size fraction.

We observe two distinct types of anomalous eutectics. One type appears at the cell edges and consists of coarse, strip- or block-shaped Cu within an Ag matrix; with this location at the cell margins clearly indicating this is the last structure to solidify. The other type is located at the centres of eutectic cells and consists of finely dispersed Cu within the Ag matrix; this likewise clearly being the first material to solidify, with the growth of the regular eutectic radiating out from these anomalous regions. Based on their morphology and spatial distribution, the anomalous eutectics at the cell edges are attributed to low undercooling conditions, while the anomalous eutectic at the cell centres is considered to result from growth at high undercooling. The formation for the low undercooling anomalous eutectic can be explained by the kinetic shift mechanism proposed by Mullis et al. [9]. The Cu dendrites observed at the cell edges, particularly in Fig. 1e, is consistent with this explanation, which results in an enrichment of Cu in the liquid ahead of the solidification front [9]. In this study, we focus on investigating the formation of the high undercooling form of the anomalous eutectic observed at the eutectic cell centres.

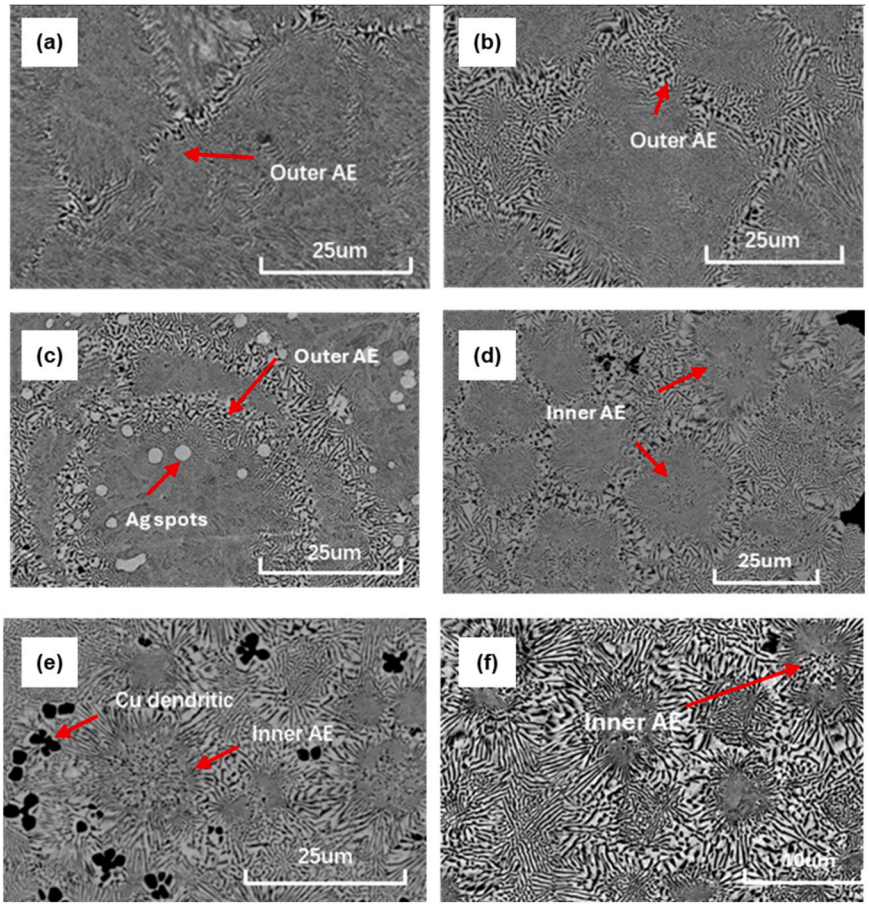

Fig. 1. BSE image of eutectic Ag-Cu droplets produced by drop-tube processing: a. 850–500 μm, b. 500–300 μm, c. 300–212 μm droplets with Ag-rich single phase regions, d. 300–212 μm droplets with high undercooling anomalous eutectic, e. 212–150 μm droplets and f. 150–106 μm droplets. The abbreviation "AE" in the figure label is Anomalous Eutectic.

Fig. 2 summarises the statistical analysis of the occurrence of inner anomalous eutectic (inner AE) as a function of droplet size. Two parameters are presented: (i) the percentage of droplets in which inner AE is observed (Pct. Occ. Inner AE), and (ii) the areal fraction of inner AE relative to the total droplet area (Pct. Area Inner AE).

Both parameters exhibit a clear dependence on droplet size. As the droplet size decreases, the probability of observing inner AE increases significantly. For example, the occurrence frequency rises from approximately 10% in droplets of 850–500 μm to about ~75% in droplets 53–38 μm. A similar trend is observed for the areal fraction of inner AE, which increases from nearly 0–1% in the largest droplets to approximately 10–15% in the smallest droplets.

It should be noted that some statistical scatter is present in the data. This scatter is expected due to the stochastic nature of nucleation and the variation in undercooling between individual droplets. Nevertheless, the overall trend clearly indicates that inner AE formation becomes increasingly probable and occupies a larger fraction of the droplet volume as the droplet size decreases. This behaviour is consistent with the higher cooling rates and larger undercoolings associated with smaller droplets.

3.2. Morphological & compositional analysis

To elucidate how these high undercooling anomalous regions are formed in the eutectic cell centres we present a detailed analysis of their morphology and composition from droplets spanning a range of different sizes. We find that the size and shape of these anomalous regions are highly variable, showing no direct correlation with droplet size. Example morphologies are shown in Fig. 3, with our manual delineation of the anomalous region superimposed. The sizes for the regions are typically of the order 5 μm, with all having an irregular highly branched morphology. In some cases the anomalous eutectic region is surrounded by a halo of Ag-rich material (most obviously in Fig. 3c) while in other cases the regular eutectic radiates directly off the anomalous material (e.g. Fig. 3d). The delineation of the anomalous region can be carried over to the SEM, wherein the average composition of the region enclosed can be determined by EDX, with this having been undertaken for all size fractions from 300 to 212 μm and smaller. For each size fraction, at least five different anomalous areas were analysed in this manner. In Fig. 3a, which corresponds to the 300–212 μm sieve fraction (i.e. likely representing the lowest undercooling among the four microstructures), where the microstructure appears to show a possible tendency toward four-fold symmetry, with guidelines added to the micrograph to assist interpretation. A similar, although less well developed, tendency may also be seen in Fig. 3b. However, such symmetry is not consistently present in all cases. For instance, Fig. 3c-d display more random branching morphologies, which are still indicative of proto-dendritic features but without a fully developed 4-fold symmetry. In this respect we note that features suggestive of a developing 4-fold symmetry are most apparent in the anomalous eutectic region at lower undercoolings and become progressively lost as the undercooling increases.

Table 1 shows the average compositions obtained from EDX mapping of the anomalous regions within droplets of size $\leq$ 300 μm. In general, the scatter is relatively low, indicating that there is no significant difference in the composition of anomalous regions across the entire range of droplet sizes. For most droplet sizes, this is true to within approximately ±1 at%, with the error bars representing the statistical variation calculated from multiple measurements of similar regions within individual droplets. However, the Cu content of the 75–53 μm droplets is slightly lower than that of the other size fractions. We also note that the measured composition is consistent with the nominal (eutectic) composition of the starting alloy.

3.3. STEM-EDX analysis

To accurately characterise the phases in the anomalous eutectic comprising the eutectic cell centres, an area was selected from such a region in a droplet from the 150–106 μm sieve fraction for FIB sectioning. This area was selected contained both the central anomalous

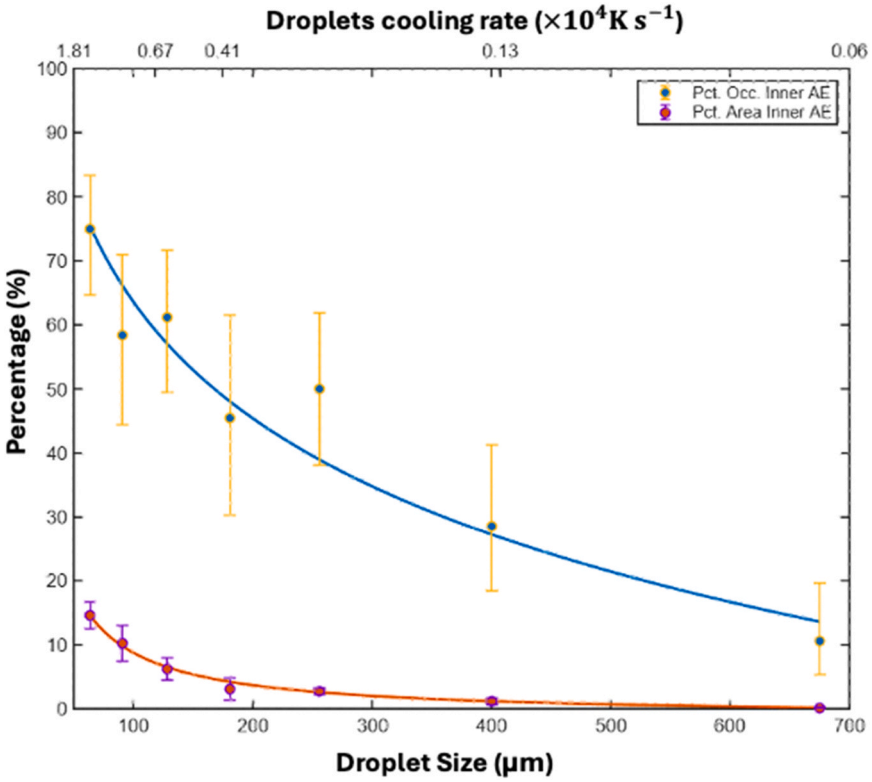

Fig. 2. Statistical occurrence and area fraction of inner anomalous eutectic as a function of droplet size and cooling rate.

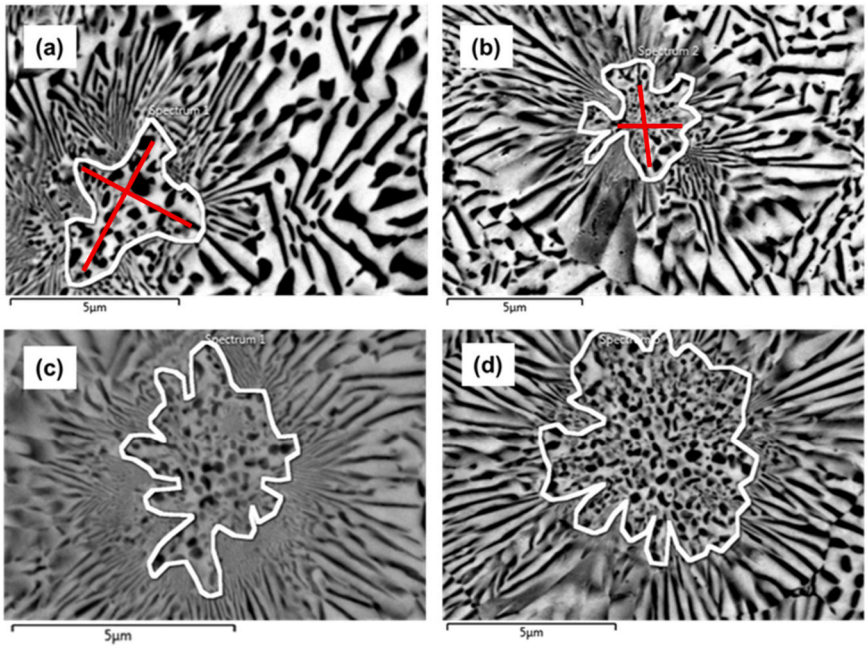

Fig. 3. Detailed view of the high undercooling anomalous eutectic morphology in drop-tube processed Ag-Cu: a. 300–212 μm, b. 212–150 μm, c. 106–75 μm, d. 75–53 μm droplets. The outline of the anomalous region has been added manually for EDX analysis of the enclosed region.

Table 1
SEM/EDX composition data for the high undercooling anomalous eutectic by droplet size fraction.

	Average droplets size/ μm						
	300 212	212 150	150 106	106 75	75 53	53 38	< 38
Cu (at%)	38.81	38.88	39.46	38.70	38.03	38.58	38.71
Ag (at%)	61.19	61.12	60.54	61.30	61.97	61.42	61.29
Standard error (at%)	±0.24	±0.38	±0.25	±0.17	±0.29	±0.23	±0.29

eutectic and the lamellar eutectic radiating from it. The resulting cross-sectional STEM bright-field image is shown in Fig. 4a. HAADF images of both the regular lamellae (Fig. 4b) and the anomalous eutectic (Fig. 4c) areas are shown, the latter comprising fine Cu-rich precipitates, less than 300 nm in size, in a matrix of Ag-rich material. It is apparent within Fig. 4a that both the Cu-rich regions within the anomalous eutectic, and the eutectic lamellae that subsequently replace this morphology, share an approximately common orientation extending radially outwards. We believe that this reflects a common nucleation point that is just beyond the top of the micrograph. The mechanism for this alignment is discussed in detail in Section 4.

Fig. 5 shows the STEM-EDX analysis of two lamellar eutectic regions with slightly different spacings of 98.2 and 121.1 nm. We find that the composition of the Ag-rich lamella is relatively uniform at 16–19 at% Cu. However, there are some differences in the composition of the Cu lamellae between the samples. The Cu lamellae in the line scan from the finer eutectic average 85–90 at% Cu, while that for the coarser eutectic averages 90–95 at% Cu, as shown in Fig. 5b and d respectively. We employ the scaling law developed by Jackson and Hunt [54] to calculate the eutectic growth rate in these samples. The specific formulae used are: $\lambda_e^2 V = \frac{K_2}{K_1}$ and $\lambda_e \Delta T_e = 2K_2$, where $K_1 = 1.54 \times 10^{10}$ Ksm^{-2} and $K_2 = 2.15 \times 10^{-7}$ Km are material-related parameters, the values for which in the Ag-Cu system are given by [12,57], while ΔT_e and λ_e are the extreme undercooling and lamellar spacing respectively. Based on these formulae and the lamellar spacing determined from Fig. 5a&c, we estimate that the average growth rates in these regions are 1.44×10^{-3}m/s and 0.94×10^{-3}m/s respectively. Consequently, we suggest that the possibility of significant solute trapping during the growth of the lamellar eutectic is relatively low, typical diffusive speeds are of the order of a few metres per second.

With reference to Fig. 5a & d, the apparent compositional transition between the Cu-rich and Ag-rich lamellae extends over approximately 25 nm. However, the spatial resolution of EDX line scans can be influenced by factors such as sectioning geometry (i.e. the interface not being parallel to the electron beam) and electron beam broadening within the specimen. Consequently, this value should be regarded as an apparent transition width rather than the intrinsic interface width. These effects may also lead to a slight underestimation of the Cu content in the Cu-rich lamellae, which is likely closer to ~90–95 at% Cu than the ~85–90 at% indicated by the EDX measurements.

The morphology of the anomalous eutectic is shown in the HAADF image in Fig. 6a, which also indicates the location of the transect used for the line scan presented in Fig. 6b. A STEM-EDX Cu map is shown in Fig. 6c, where the letters A–E mark the locations of five point composition measurements, the results of which are listed in Table 2. The EDX measurements indicate that the Cu-rich dispersions within the anomalous material typically contain 92–94 at% Cu, and are embedded within an Ag-rich matrix containing approximately 20–26 at% Cu. In addition, the compositional transition observed in the line scan between the Cu-lean and Cu-rich regions appears sharper than that observed for the lamellar eutectic, typically on the order of ~10 nm.

3.4. 4D-STEM orientation map

Fig. 7 shows the orientation and phase maps obtained from 4D-STEM for a region displaying this inner anomalous eutectic morphology. The x and y axes correspond to the in-plane scanning directions, whereas the z axis represents the projection along the electron-beam direction. The x, y, and z directions used for the orientation maps are defined by the specimen coordinate frame shown in Fig. 7 f, while the colour key is given by the inverse pole figure (IPF) shown in Fig. 7e. Fig. 7 g also presents data from the Z-axis orientation map, but now only for the Cu-rich phase. This, combined with the distribution of misorientation angles for these Cu-rich regions, as given in Fig. 7 h, clearly indicates a

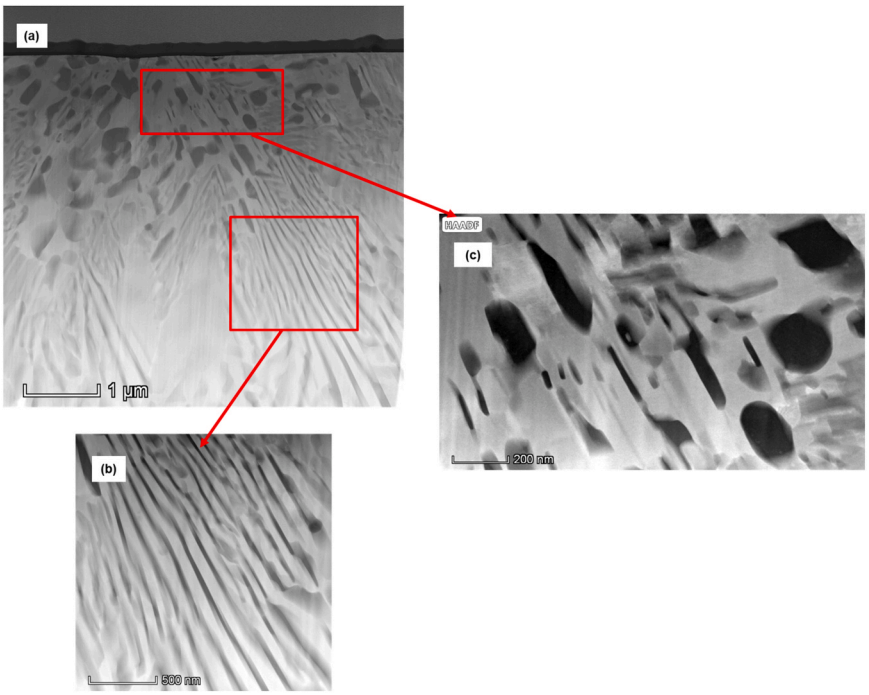

Fig. 4. Microstructure of a 150–106 μm droplet: a. eutectic cell centre STEM bright-field image, b. HAADF image of anomalous eutectic, c. HAADF image of regular lamellar eutectic.

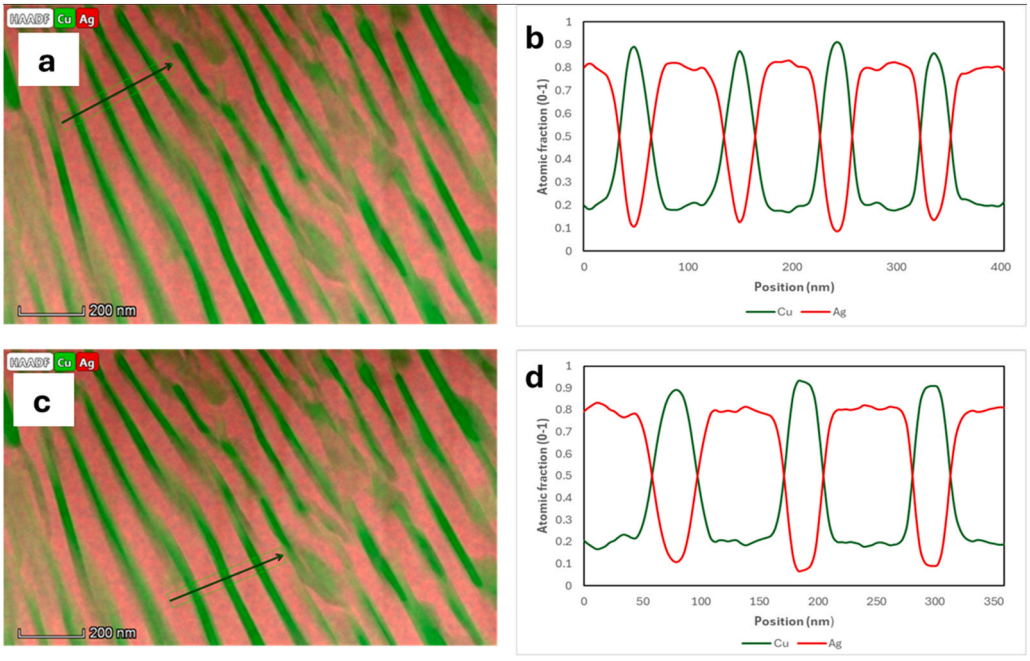

Fig. 5. STEM-EDX analysis of lamellar eutectic from the 150–106 μm drop-tube sample (red= Ag and green = Cu): a. STEM-EDX map, finer lamellar area, with location of line scan indicated; b. Line scan, finer lamellar area; c. STEM-EDX map, coarser lamellar area, with location of line scan indicated; d. Line scan, coarser lamellar area.

strong textural relationship between these spatially isolated Cu-rich grains, with misorientation angles clustering around 0°, 30° and 60°. These misorientation angles are measured relative to the largest Cu-rich grain, which is labelled in the figure.

In addition, the local misorientation distribution between neighbouring pixels at the Cu-Ag phase boundaries was analysed using the orientation data obtained from the 4D-STEM measurements. For each pixel, the misorientation angle was calculated by comparing its crystallographic orientation with those of its eight neighbouring pixels. The spatial distribution of the misorientation is shown in Fig. 7i, where the coloured boundaries indicate orientation differences between adjacent pixels. The corresponding statistical distribution of the Ag–Cu interfacial misorientation angles is presented in Fig. 7j. The histogram shows that a large fraction of the misorientation angles are concentrated near ~60°, while another population occurs at low misorientation angles (0–5°). Only a small fraction of interfaces exhibits intermediate

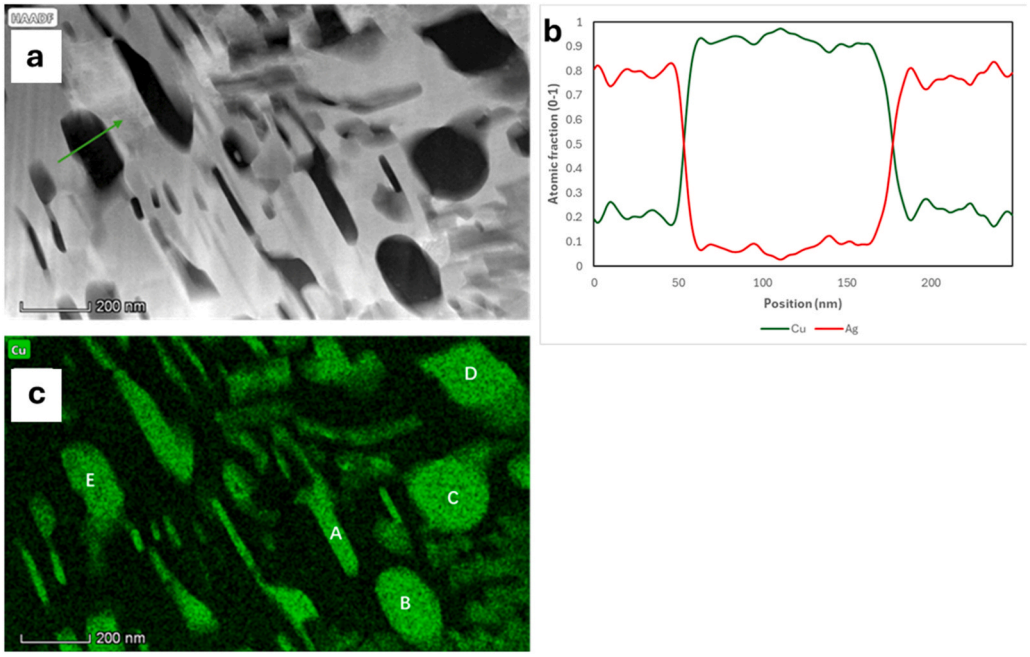

Fig. 6. STEM-EDX analysis of anomalous eutectic from the 150–106 μm drop-tube sample: a. HAADF image, b. EDX line scan across one Cu-rich dispersoid, the location of which is indicated by the line in part a; c. STEM-EDX Cu-map from area scan.

Table 2
EDX data of Cu-rich dispersion phase of 150–106μm droplets produced by drop-tube.

	A	B	C	D	E
Cu (at%)	93.2 ± 0.05	93.3 ± 0.5	94.3 ± 0.3	94.1 ± 0.3	92.1 ± 0.3

misorientation angles.

3.5. Cooling rate and undercooling simulation results

Fig. 8a shows the estimated relationship between undercooling and droplet size as evaluated by Eqs. (1) and (2). For the size range of 850–53 μm, the undercooling ranges between 10 and 210 K, with undercooling increasing as droplet size decreases. The simulation predicts that the undercooling required to first drop below the T_0 temperature (76 K) is achieved in the 300–212 μm sieve size fraction, with the average undercooling for this droplet size being 86 K. This droplet size range is therefore considered a transitional regime. This interpretation is supported by the microstructural observations. In particular, Ag dendritic regions were first observed in droplets within the 300–212 μm size range, where they coexist with central anomalous eutectic structures. In contrast, droplets larger than 300 μm do not exhibit such features.

Previous studies have reported that the critical undercooling required for eutectic decoupling in the Ag–Cu system is 70 K. Therefore, the undercooling of droplets in the 500–300 μm size range is expected to remain below this value. Based on these experimental observations and literature constraints, the model parameters were varied to provide a reasonable range of simulated undercooling values. The error bars shown in Fig. 8a therefore reflect the variation in undercooling associated with this sensitivity analysis. This constraint is illustrated by the horizontal line at $\Delta T = 70$ K in Fig. 8a. The parameter range selected is such that all undercoolings within the 500–300 μm size fraction remain below $\Delta T = 70$ K, while those in the 300–212 μm size fraction are above this threshold. By far the most widely varying parameter is K_v, which is constraint in this way to the range 10^{50} - 10^{34} m^{-3} s^{-1} .

Based on the previously obtained ΔT, the explicit Euler method was applied to calculate the temperature–time evolution for droplets of different sizes. Taking droplets with diameters of 75–53 μm as an example, the results are shown in Fig. 8b. The undercooling is approximately 210 K, and the plateau stage lasts for about 0.012 s. We use the cooling rate after complete solidification to represent the relationship between droplet size and characteristic cooling rate, as indicated by the orange tangent line in Fig. 8b. In addition, the Supplementary information provides the cooling rate as a function of time for a typical droplet in this size fraction.

The characteristic cooling rate, as a function of droplet diameter, is shown in Fig. 8c for droplets in the 850–53 μm size range, wherein cooling rates range from 470 to 28000 K s^{-1}. Erol et al. [48] have also estimated cooling rates of eutectic Ag Cu alloy in the drop-tube, finding the same general trend as observed here, albeit their estimated cooling rates were somewhat higher due to the use of helium as a backfill gas, rather than nitrogen as in our experiment. The relationship between the cooling rate and the droplet diameter is well fitted via a power law expression:

$$\frac{dT}{dt} = 0.0245 \times d^{-1.439} \quad (7)$$

Where both d and $\frac{dT}{dt}$ are in standard SI units. This relationship is also shown in Fig. 8c

3.6. Nucleation incubation time for Ag and Cu

Based on Eq. (4), the calculation of nucleation incubation time for the Ag and Cu phases as a function of undercooling is shown in Fig. 9. As undercooling increases, the difference between the nucleation times of Ag and Cu gradually becomes more pronounced. Across all undercooling ranges, the nucleation time of Cu is consistently estimated to be lower than that of Ag. This suggests that, with increasing undercooling, Cu becomes more likely to nucleate in preference to Ag. However, Shao et al. [51] point out a potential shortcoming in the viscosity estimate used in this calculation. The pre-exponential factor in the Arrhenius type expression is measured above the melting point, which may cause significant deviation for deeply undercooled melts. Therefore, the possibility that Ag nucleates in preference to Cu cannot be excluded if the difference in nucleation times between Ag and Cu is relatively small.

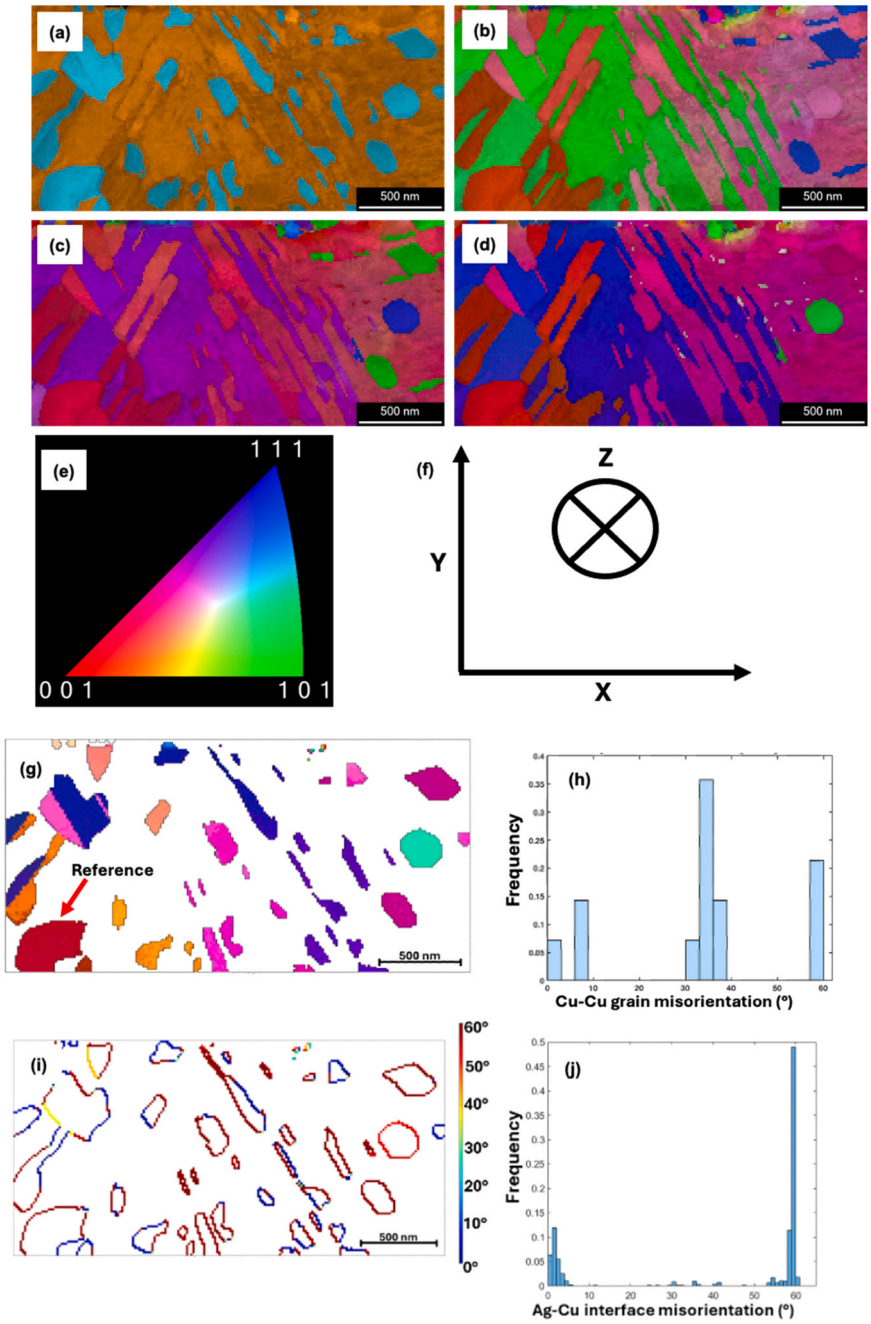

Fig. 7. a. Phase map of the anomalous eutectic, where blue denotes Cu and yellow denotes Ag, obtained from the 150–106 μm drop-tube sample; b. X-axis orientation map and corresponding IPF for the Ag–Cu anomalous eutectic; c. Y-axis orientation map; d. Z-axis (beam-direction) orientation map; e. inverse pole figure; f. Sample coordinate frame; g. orientation map of Cu phase (beam direction); h. histogram of Cu grain misorientation angles with reference of largest grain i. Spatial distribution of Ag–Cu interfacial misorientation; j. histogram of Ag–Cu interfacial misorientation angles.

More detail is given in Supplementary Information, together with the wetting angles for both Ag and Cu, which we take to be different.

3.7. Solidification growth rates

We used the LZ model and LKT models to simulate the relationship between growth rate and undercooling for the eutectic and single phase dendrites (Ag- & Cu-rich phases) respectively, with the results being given in Fig. 10. The growth rate of Ag dendrites exceeds that of the eutectic at an undercooling of approximately 70 K, which is consistent with both our experimental observations and previous work in the literature. We also note that the simulated growth rate of Cu dendrites is significantly slower than that of the Ag dendrites over the whole undercooling range studied. This appears to be due to strong partitioning of Ag from the Cu-rich solid in our simulations ($k_E = 0.083$), coupled with the high Ag concentration in the melt at the eutectic temperature, which results in a high solutal undercooling, slowing growth. However, simulations by Zhao et al. [47] found that dendritic Ag and Cu exhibit very similar growth rates, with Cu showing a relatively high growth rate. This is clearly inconsistent with our experimental observations. We believe that this discrepancy may arise from the fact that the effect of the phase diagram was not considered in the application of the LKT model by Zhao et al. [47].

Following Goetzinger et al. [58], who used the LKT model to simulate thermally controlled single-phase growth, we also estimate the growth rate of the partitionless solid. In this case, the undercooling used

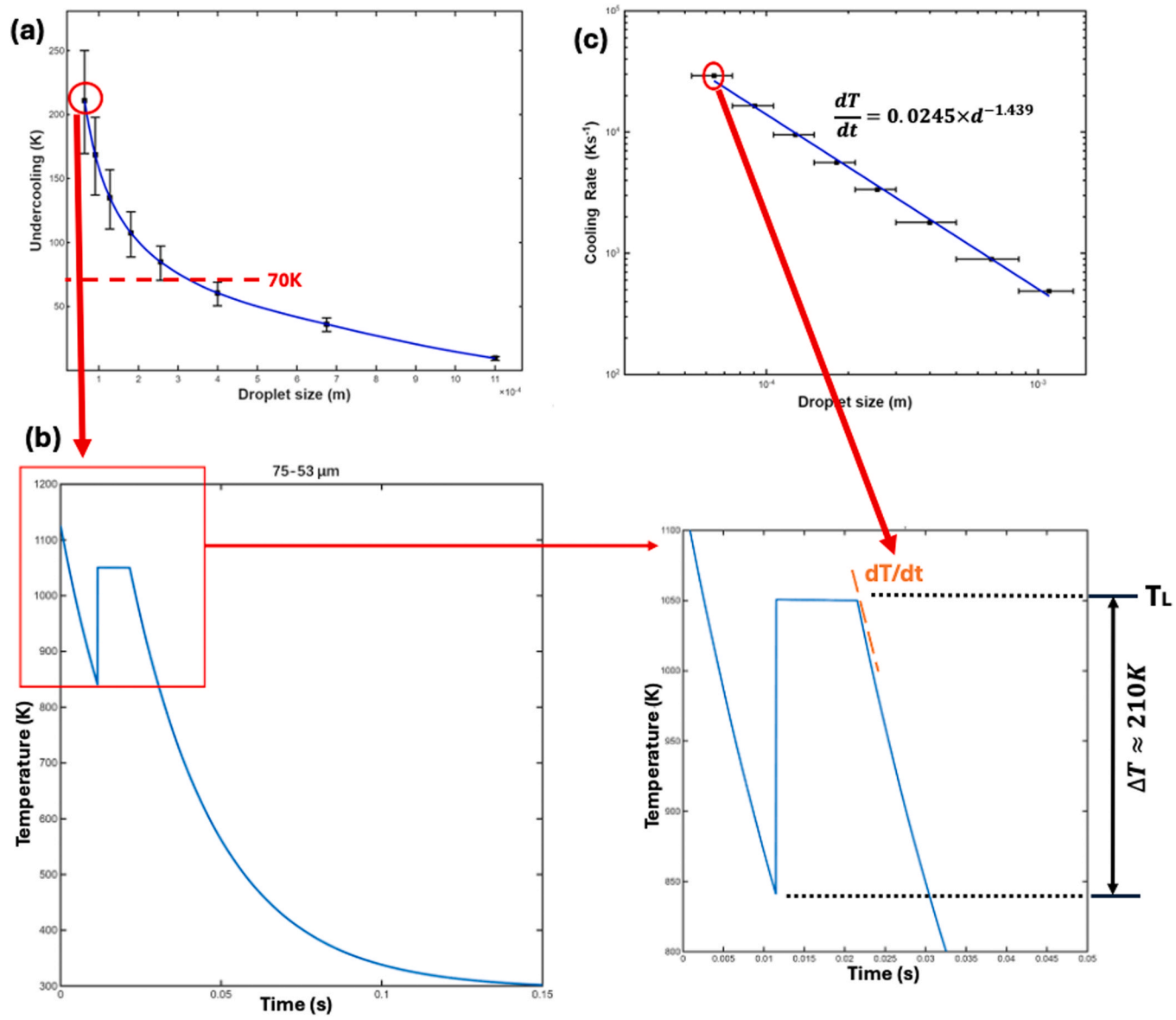

Fig. 8. a. Estimated undercooling of drop-tube processed Ag-Cu alloy as a function of droplet size, b. simulated temperature-time profile for an example droplet in the 75–53 µm size range with undercooling as given in part (a) and cooling rate, immediately post-recalescence, which is used in part (c) of the figure, c. characteristic cooling rate of Ag-Cu alloy in drop-tube as a function of droplet size.

in the model is the depression below the T_0 temperature, not below the liquidus, although for consistency we report the undercooling as depression below the liquidus. Accordingly, at an undercooling of approximately 90 K (around 14 K below T_0), the growth rates of the partitionless solid exceed that of Ag-rich dendrites, with the growth rate continuing to increase rapidly with undercooling, reaching 1 m s^{-1} in just tens of K, far exceeding the growth rate of the Ag- & Cu-rich dendritic solids subject to normal partitioning. In addition, because the LZ model used to calculate the eutectic growth rate assumes that the partition coefficient is the same in both phases ($k = k_\alpha = k_\beta$), we recalculated the model using the individual values of k_α and k_β to determine the corresponding error bar. The deviation in the calculated growth velocities is negligible for undercoolings below approximately 150 K.

4. Discussion

The morphologies of various anomalous eutectic structures have been reported in the literature [3,4,11]. Based on previous studies and our experimental results, these structures can be roughly categorized into two categories: those formed under low undercooling conditions and those formed under high undercooling conditions, wherein the working assumption would be that different formation mechanisms are giving rise to these structures.

Through our experimental observations we have identified two different forms of anomalous eutectic structures in Ag-Cu eutectic cells. Coarse blocky or strip eutectic structures were found at the edge of the cell, which we attribute to a kinetic shift of the eutectic point during rapid solidification leading to Cu-enrichment of the last liquid to solidify, as proposed by Mullis & Clopet [9]. In contrast, the anomalous material located in the cell centres is composed of a very fine dispersion of Cu-rich precipitates in an Ag-rich matrix. The location of this material at the eutectic cell centres, together with its occurrence in only the smaller droplet sizes, leads us to conclude this is a high undercooling morphology.

However, before exploring phase decomposition as the origin of this anomalous eutectic morphology, we list several phenomena that also require explanation:

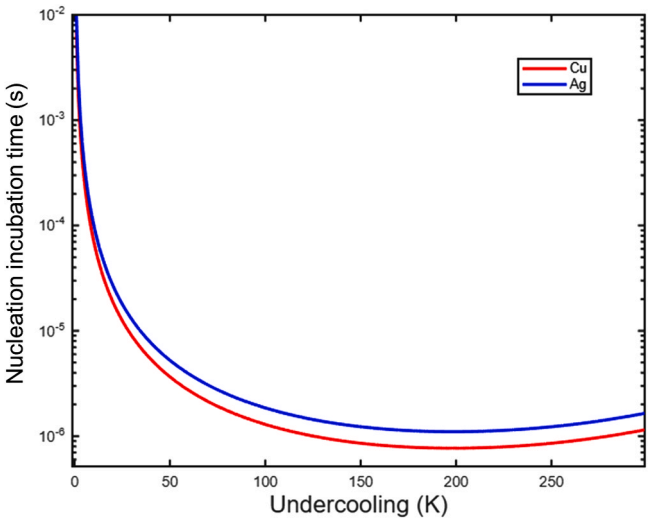

Fig. 9. Estimated nucleation incubation time for Ag and Cu as function of undercooling.

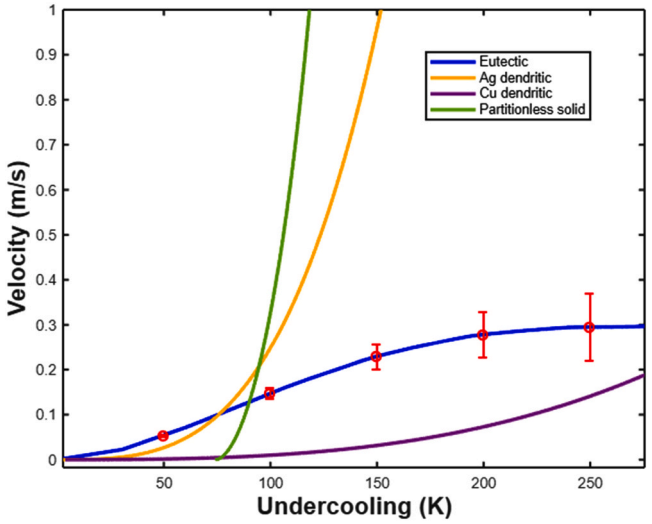

Fig. 10. Estimated growth rate as function of undercooling.

1. Within any given droplet size range, certain droplets exhibit anomalous eutectic structures, whereas others do not. In particular, when the droplet size is below 300 μm, the occurrence frequency of anomalous eutectic structures in the central region increases noticeably, whereas such structures are rarely observed in droplets larger than 300 μm.
2. The anomalous eutectic in droplets < 300 μm in diameter does not appear in every eutectic cell within the droplet, with some cells maintaining the regular lamellar morphology throughout.
3. In droplets within the 300–212 μm size range, single phase Ag-rich regions may appear in some droplets, with anomalous eutectic being observed in others.

In the drop-tube experiment, although the cooling rate of the droplets is deterministic, the undercooling of the droplets before solidification is stochastic. This implies that droplets of similar sizes have comparable cooling rates but may exhibit different degrees of undercooling. Melt subdivision reduces the distribution of impurities and potentially eliminating heterogeneous nucleation sites in some droplets. Therefore, in general, smaller droplets exhibit higher undercooling [23,42,59,60], however, lower undercooling in small droplets is not impossible. Conversely, a limited number of larger droplets may also attain high undercooling. Similarly, within a single droplet, depending upon the potency of different heterogeneous nuclei, different eutectic cells may nucleate at different undercoolings. Assuming there is a critical undercooling which must be exceeded for the formation of the anomalous eutectic, we may therefore observe some cells containing anomalous structure at their centres, and some not. The only caveat here is that each such region should be sufficiently separated from any others that there is no overlap of the thermal fields, i.e. that recalescence from one region does not start to warm and hence inhibit nucleation of its neighbours. Consequently, this natural variability in undercooling, both between droplets and within droplets, is likely to explain most, if not all, of the variability observed, irrespective of the mechanism for the formation of the anomalous eutectic. In addition, it should also be noted that the observations are based on two-dimensional cross-sections of the droplets. As a result, in some particles the anomalous eutectic may not be intersected by the examined section and therefore may not be visible in the micrographs. The statistical data presented in Fig. 2 provide strong support for the above argument.

We consider now in turn the possible mechanisms for the formation of this high undercooling anomalous eutectic, including remelting, decoupled growth of the two phases and phase decomposition, starting with remelting. We note first that if remelting had occurred, the material in the as-solidified sample would have reformed close to equilibrium, meaning its composition should approach the metastable extension of the solidus, potentially at an undercooling just below the eutectic temperature. However, based on the compositions determined by STEM-EDX, and the solubility around equilibrium which is predicted from the CALPHAD thermodynamic database and literature [45], this scenario seems implausible. Indeed, irrespective of the undercooling assumed for growth, the compositions of both the Ag- and Cu-rich phases fall well inside the metastable extensions of the two solidus lines. Remelting is also usually accompanied by coarsening, yet at least part of the Cu-rich phase is smaller than the eutectic scale. Moreover, if we assume partial remelting, with some fragmented remnants of the Cu-rich phase being retained, these would tend to adopt random orientations. As Liu et al. [61] reported, the orientation of resolidified fragments tends to become more random with increasing undercooling. This cannot account for the orientation map obtained from our 4D-STEM data, as shown in Fig. 7 in which Cu-rich grains display orientations with respect to each other which cluster around 0°, 30° and 60°, rather than displaying the broad maximum around 45° characteristic of the Makenzie distribution for randomly oriented grains in cubic metals. Remelting also appears incompatible with the thermal history calculations presented in Fig. 11, wherein even if remelting does occur, it will do so at the end of recalescence during the isothermal plateau, with this being likely to affect the lamellar eutectic surrounding the anomalous material, rather than the anomalous eutectic at the cell centre. Finally, we note that melting generally smooth out irregular boundaries, whereas the irregular interfaces between anomalous regions and lamellae, as shown in Fig. 3, are more consistent with a growth-driven mechanism, a point we will return to below.

This is contrary to a number of other studies [1,17–19] which have suggested just such models based upon decoupled growth and dendrite fragmentation for the origin of the anomalous eutectic under deep undercooling. However, many such investigation have been conducted via injection casting/EM levitation (e.g. [24,62]), wherein the suspended melt is strongly stirred due to electromagnetically induced convection, promoting the occurrence of fragmentation. Such stirring effects are absent in drop-tube and glass fluxing techniques. Moreover, the duration of the isothermal plateau, during which remelting could occur, is significantly curtailed in droptube experiments.

Turning now to decoupled growth of the Cu- and Ag-rich phases, if such a mechanism were to operate we would conclude from the morphology of the anomalous regions that the Cu-rich phase would be the first to nucleate, followed by in-fill of the Ag-rich matrix. As

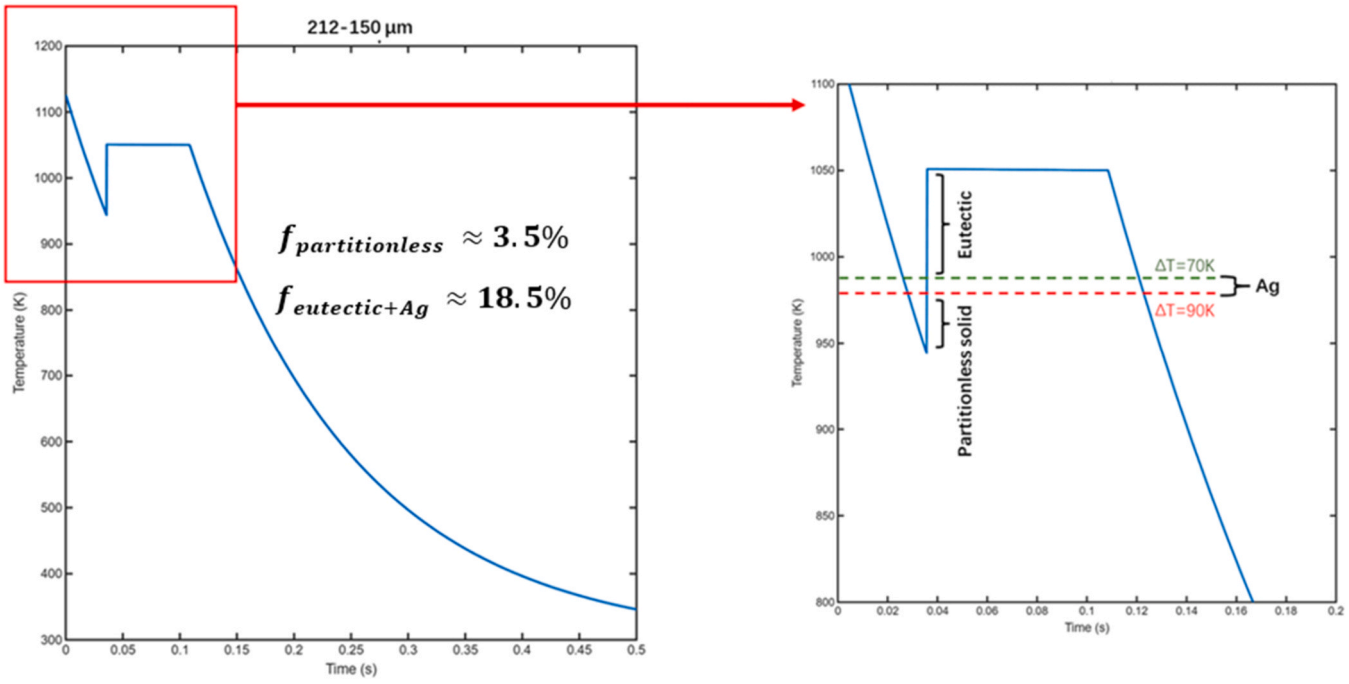

Fig. 11. Temperature-time relation for droplets 212–150 µm.

indicated by the nucleation incubation time calculation presented in Fig. 9, this scenario appears feasible. However, such a fine structure as that observed would require an exceptionally high nucleation rate. As with remelting, the compositions in this case should lie on the metastable extension of the solidus lines, albeit at potentially much higher undercooling. Consequently, with reference to Fig. 12, the same objection may be raised, namely that the measured compositions cannot be reconciled with the metastable extensions of the two solidus lines, irrespective of the undercooling assumed. Moreover, the 4D-STEM data raises the same objections as for the remelting model. If Cu had nucleated independently, random orientations would be expected, which is not what is observed. Moreover, it is likely that multiple Cu-rich regions nucleated independently at high undercooling would exhibit dendritic morphologies. Yet, as shown in Fig. 7, many Cu-rich regions clearly display facets. Finally, it is difficult to see why, if decoupled growth is assumed, that the volume fraction of the anomalous region is so small.

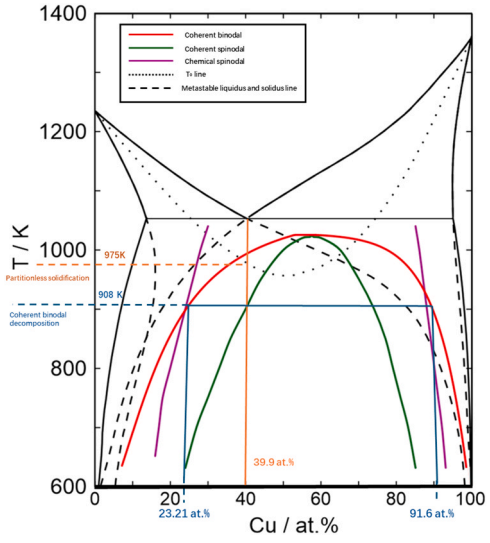

Fig. 12. Ag-Cu phase diagram incorporating metastable solidus and liquidus extensions, T_0-line, estimated coherent binode and chemical & coherent spinode.

Previous studies [45] have shown that the enthalpy of mixing of the Ag–Cu system is positive in both the liquid and solid states. As the temperature decreases, the entropic contribution ($T \bullet \Delta S_{mix}$) to the Gibbs free energy is therefore reduced, increasing the likelihood of phase separation within the system. Consequently, here we explore the prospect that the high undercooling anomalous eutectic morphology arises from a phase separation phenomenon. This could be direct from the liquid, or alternatively, given the low undercooling required to access the T_0 temperature, could be in the solid state with the precursor for this being a single phase solid at the eutectic composition

having formed via partitionless solidification.

The metastable extensions of the Ag-Cu binary phase diagram are well-established through e.g. the work of Subramanian et al. [45] and others. From this we can assess that the Ag-Cu eutectic alloy requires an undercooling of approximately 238 K to achieve metastable liquid phase separation. However, if homogeneous nucleation of the crystalline phase occurs before reaching this level of undercooling, LPS (liquid phase separation) becomes very unlikely. Walder and Ryder [11], utilizing the data of Solthin and Chadwick [63], determined the homogeneous nucleation temperature and incorporated it into the phase diagram, finding that $T_{homogeneous}$ is approximately 40 K higher than the onset of the metastable liquid miscibility gap. Consequently, the likelihood is that solidification occurs before the liquid undercooling reaches the metastable liquid miscibility gap, preventing LPS from occurring at this composition. We also note that the high undercooling required for liquid phase separation would, based upon the calculation presented in Fig. 8b, not be compatible with the formation of anomalous eutectic in the 300–212 µm size fraction via a liquid phase separation route. Moreover, as seen in Fig. 7g-h, the Cu-rich precipitates, despite being spatially isolated, display a strong texture with misorientation angles clustering around 0°, 30° and 60°. For regions forming via liquid phase separation and then solidifying independently, it is difficult to envisage how such an arrangement of orientations might come about. Coalescence of the droplets of the minority phase liquid is also likely to mean that structures formed via LPS are quite coarse, inconsistent with the fine structures observed here.

We therefore consider the possibility that the anomalous eutectic located in the eutectic cell centres (as shown in Fig. 1) originates from a solid-state decomposition reaction. Specifically, that the initial solidification is to a single phase solid that then decomposes to give the observed anomalous eutectic structure. In this regard we note that the composition of the anomalous eutectic, when averaged over the Ag-rich matrix and Cu-rich inclusions, is independent of the droplet size fraction (as a proxy for undercooling) and equal to the notional composition of the liquid, as shown in Table 1. As such, if the precursor of this anomalous eutectic morphology is a single phase supersaturated solid-solution, it is one with the same composition as the eutectic. This is not consistent with solute enrichment via kinetic solute trapping [27,33,64], wherein we would expect a progressively more supersaturated solid-solution as the undercooling, and hence growth velocity, increased. In fact, this looks more like the binary transition from equilibrium partitioning to full thermodynamic partitionless solidification as reported by Teggin et al. [42]. This is equivalent to the step-change behaviour in partitioning behaviour proposed by Eckler et al. [36], with a critical undercooling defined by that required to drop below the T_0 temperature. Additional support for this interpretation comes from the crystallographic characteristics of the phases produced by the subsequent solid-state decomposition. In particular, the strong crystallographic texture revealed by the 4D-STEM data in Fig. 7 is consistent with the Cu phase originating from the solid-state decomposition of a common precursor phase. This point is discussed in further detail in the following analysis. This is discussed in more detail below.

According to numerous studies [9,11,12,24], decoupled growth of Ag dendrites occurs at an undercooling of approximately 70 K, slightly above the T_0 temperature. This suggests that the sequence of microstructural evolution with increasing undercooling is: regular lamellae → single-phase Ag dendrites → partitionless solidification, noting that as growth proceeds the droplet may be continuously warming wherein, particularly near the onset temperature for a growth transition, these morphologies may be restricted to a relatively small area within a droplet. This trend is consistent with the structures observed in our experiments, particularly the very narrow droplet size (undercooling) interval in which single-phase Ag dendrites appear. We only briefly observed such precursor Ag dendrites in droplets with sizes ranging from 300 to 212 μm; they were rarely observed in droplets of other size ranges. Although, as shown in Fig. 9, in our simulations the Cu nucleation time is marginally shorter than the Ag nucleation time at all undercoolings, the growth velocity for Ag-rich dendrites so significantly outpaces that for Cu-rich dendrites, we expect that the growth of Ag-rich dendrites will dominate, as observed. Specifically, given the FCC structure of both phases, we would expect that even if Cu were to nucleate first, this would quickly nucleate and then be overgrown by the much faster growing Ag-rich phase, in line with both our observations and those reported extensively by other workers [9,11,12,24].

Returning to the growth of the partitionless solid, as shown in Fig. 10, this benefits from a significant growth velocity advantage, since it does not require the rejection of solute with its growth being rate limited by thermal diffusion only. Specifically, the partitionless solid will outgrow either the eutectic or Ag-rich single-phase dendrites at all undercoolings in excess of 90 K, as measured from the liquidus temperature, albeit it is the depression of the temperature below T_0 that determines the growth rate of the partitionless solid. This growth advantage becomes progressively greater as the undercooling is increased.

Example Temperature–time curves of droplets were calculated using the explicit Euler method, as shown in Fig. 11. Here, droplets with diameter in the range 212–150 μm are taken as an example. Although the temperature is below T_0, the undercooling relative to T_0 is small. Initially, a partitionless solid will grow but the release of latent heat from this growth will rapidly warm the droplet. When the undercooling is reduced to 90 K, the partitionless solid will be replaced by single phase Ag. This is because, for $\Delta T < 90$ K single phase Ag can outgrow the partitionless solid (see Fig. 10) and will result a thin halo of Ag separating the partitionless solid from the lamellar eutectic. The volume fraction of the partitionless solid is given by $f = c_p\Delta T^*/L$, where $\Delta T^* = T_E - 90 - T_{nuc}$. This gives a fraction solid for the partitionless material of 3.5% in this case, while the total solid fraction formed before the plateau stage is around 22%. Due to the extremely high cooling rate and heat transfer efficiency in the drop-tube, the plateau duration for droplets in this size fraction is only around 0.08 s (and less for smaller droplets), making large-scale remelting unlikely. Moreover, even if remelting occurs, it will take place after recalescence and preferentially melt the outer eutectic rather than the inner partitionless solid.

From the above discussion, we consider that a partitionless single-phase solid growing at a temperature below T_0 and with the eutectic composition is a potential precursor for the high undercooling anomalous eutectic. Consequently, the mechanism responsible for the subsequent decomposition of this single phase solid and the formation of the observed anomalous eutectic also requires discussion. Just as with the liquid phase, a miscibility gap has been identified in the solid-state [65].

In the liquid phase, wherein phase separation does not generate internal strain, the miscibility gap is determined by the chemical binode or spinode. However, in most metallic solids, the variations of the lattice parameter will introduce corresponding elastic strain. Additional undercooling is required to overcome the elastic energy associated with this strain, shifting the binode and spinode to lower temperatures, wherein they are termed the coherent binode or spinode [66].

To evaluate the locus of the phase separation region we evaluate the Gibbs free energy curve for the alloy as a function of composition and for a range of different temperatures, both with and without the elastic energy contribution arising from the difference in lattice spacing due to the compositional difference. We use the common tangent method to precisely locate two compositions on the free energy curve from which we can construct the locus of the chemical & coherent binodal lines. The spinodal region is determined by the position of the second derivative from the points of inflection, $\frac{d^2G}{dc^2} = 0$ of the Gibbs free energy curves for the solid solution. The chemical and coherent spinode for the Ag-Cu system was mapped, yielding a close agreement with previous studies [45,67]. We could not find a previous determination of the coherent binode lines in the literature but given that the underlying data is common between the binode and the spinode, the close agreement of the spinode with previous estimates gives us confidence in these determinations. Further details of the computational procedure is given in the Supplementary Information.

The results of this calculation are given in Fig. 12. A miscibility gap in the solid is predicted across most of the composition range. In Fig. 12 the red curve represents the coherent binodal, the green curve corresponds to the coherent spinode, and the two purple curves denote the segments of the chemical spinode below the eutectic temperature. For an alloy of eutectic composition (39.9 at% Cu), binodal decomposition could occur between 975 K, above which the partitionless solid cannot form as we are above T_0, and 900 K, below which spinodal decomposition is predicted. Within this temperature range, phase separation proceeds via a nucleation and growth mechanisms. Below 900 K, phase separation is expected to occur through spontaneous coherent spinodal decomposition. The actual mechanism likely to be operating is discussed further below, based upon the morphology of the Cu-rich precipitates.

As shown in Fig. 7, the Cu-rich precipitates are typically 30 to $>$ 300 nm in diameter, with faceted or semi-faceted interfaces frequently observed between the Ag- and Cu-rich phases. Such faceting would generally be considered indicative of a semi-coherent or incoherent interface, with this to be expected given the considerable (≈12%) mismatch in lattice parameter between Ag and Cu. Fig. 7 also indicates a strong textural relationship between the individual Cu-rich precipitates and between the precipitates and matrix. Indeed, the combination of 0°, 30° and 60° misorientations between individual precipitates and 0° and 60° misorientations between precipitates and matrix is a textbook case

of a symmetry-breaking solid-state transformation from a single precursor phase with variant selection. Even in the absence of other evidence, the most likely scenario giving rise to such orientation relationships would be an fcc → fcc decomposition reaction with minimal lattice reconstruction and elastic strain accommodation via variant formation. Furthermore, the predominance of 60° misorientation between matrix and precipitate is indicative of a Σ3 coincidence site lattice (CSL)-type crystallographic relationship, this representing a low-energy boundary commonly observed in fcc systems.

The observations indicate that we are observing CL (coherency loss) upon decomposition, with this usually accompanied by the release of elastic energy and an increase in interface energy due to the introduction of defects, ultimately leading to changes in the morphology of the precipitates [68]. Several explanations have been proposed for the loss of interface coherence. Weatherly [69] suggested that severe lattice mismatch (typically greater than 5%) promotes loss of coherence. Cheng et al. [68] proposed that the surface energy scales with the square of the particle size; thus, when the particle size exceeds a critical threshold, the elastic energy overcomes the surface energy, making coherence loss thermodynamically favourable. Other study [70] have reported that dislocations in the matrix may also contribute to CL.

Based on previous observations, the Cu dispersions range in size from approximately 30 to > 300 nm in diameter. The Cu-rich precipitates observed resemble binodal decomposition rather than spinodal decomposition. The size range of the Cu-rich precipitates spans almost an order of magnitude, which is inconsistent with the relatively uniform compositional modulation typically associated with spinodal decomposition. Similarly, the large size of the largest precipitates is atypical for spinodal decomposition. In addition, no obviously interconnected structures, which might be expected from a spinodal decomposition mechanism, are observed. Consequently, we believe that the majority of the observed precipitates, certainly the larger ones, arise from binodal decomposition via a nucleation and growth mechanism. That said, there is also the possibility that if some regions of the partitionless solid fail to nucleate Cu-rich regions, upon further cooling the spinodal boundary will be crossed, leading to spontaneous decomposition. This process may result in the formation of very fine Cu precipitates filling the spaces between larger precipitates.

The closest match to the experimentally measured compositions for the Ag- and Cu-rich material would occur via binodal decomposition at a temperature around 908 K, with these values being indicated on Fig. 12. We note in this regard that due to the stochastic nature of nucleation the onset for the transition could occur randomly at any point within the interval 975–900 K, although it actually appears to have occurred very close to the coherent spinode, which would correspond to the point at which the driving force for a nucleated transition is close to a maximum.

Based on the above discussion, we propose that the formation of the high undercooling anomalous eutectic regions located at the eutectic cell centres in Ag-Cu does not originate from the mechanisms traditionally proposed for such morphologies, such as remelting or decoupled growth. Instead, it arises from partitionless solidification below the T_0 temperature, followed by solid-state phase separation during subsequent cooling. The formation of the partitionless solid appears to be thermodynamically, rather than kinetically, controlled with there being an apparent step change in partitioning behaviour from equilibrium partitioning to fully partitionless growth with no intermediate compositions observed.

Based on the macroscopic distribution of the Cu-rich phase, the particle size distribution and interface structure and composition data as determined by TEM-EDX data, binodal decomposition appears to be the dominant phase separation process, although some very fine Cu particles may have originated from spontaneous spinodal decomposition. Therefore, we conclude that the anomalous eutectic-like structure formed in the central region results from solid-state decomposition of the partitionless solid.

We note that in some cases there is significant spatial alignment between the dispersoids and the surrounding eutectic lamellae and this is attributed to the fact that, during growth of the partitionless region, the crystal growth direction is aligned with the direction of heat flow as latent heat is released [71]. From the initial nucleation point, the partitionless solid first grows radially outward along the direction of thermal diffusion. However, this is an unstable morphology and as growth proceeds the partitionless solid will start to develop into either a proto-dendritic morphology or a randomly branched solid, depending upon the level of undercooling, with random branching being favoured at higher undercooling. This is in line with experimental and theoretical evidence that high undercooling mediates a transition from dendritic growth along well-defined crystallographic directions (<100 > in FCC metals [72]), to dense-branched structures such as “dendritic seaweed” [73]. Evidence for this is seen in the boundary delineating the transition from the anomalous eutectic, i.e. the outer extent of partitionless solid growth, and the lamellar eutectic. At lower undercoolings, some evidence of preferred 4-fold growth is apparent, with this becoming more akin to random branching at high undercooling. We also note that the random branching of this interface is more reminiscent of a growth interface than of a remelting interface.

Once partitionless growth ceases, eutectic growth begins. This growth is also expected to initially proceed approximately radially outward from the original nucleation point, due to both alignment with the heat flow direction and due to preferential nucleation of the eutectic lamellae on the (100) planes of the partitionless solid. Finally, upon completion of solidification and subsequent cooling, the partitionless solid undergoes binodal decomposition in the temperature range 975 – 900 K, with spinodal decomposition removing any residual supersaturation at 900 K. Both processes will form Cu-rich dispersoids within an Ag-rich matrix, albeit with different sizes, which would account for the wide range of dispersoid size occurring. As is expected during a solid-state decomposition, the crystallography of the precursor will influence that of the newly formed phases, accounting for both the common orientation of many of the spatially separated Cu-rich dispersoids, as observed in Fig. 7 and, where the dispersoids are elongated the apparent alignment of these with the outwardly radiating eutectic lamellae, as noted in relation to Fig. 4. Gusakov et al. [38] also pointed out that the apparent similarity of such structures does not necessarily indicate that it originates from coupled eutectic growth. A schematic of the solidification sequence is shown in Fig. 13.

5. Summary & conclusions

We conducted a microstructural analysis of eutectic Ag–Cu alloys solidified at cooling rates of 470–28,400 K s^{-1} . Anomalous eutectic-like structures were observed in the central regions of some droplet cells. Simulated undercooling, microstructural characteristics, and growth rates of the Ag–Cu alloy system show a high degree of consistency, suggesting that these structures are associated with partitionless solidification below the T_0 temperature. Orientation mapping, TEM-EDX, and 4D-STEM analyses further support an interpretation in which the observed microstructures at the eutectic cell centres are consistent with coherent binodal decomposition of a partitionless solid.

The results of this study offer new insights into the complex solidification behaviour of undercooled eutectic melts. In particular, they indicate that anomalous eutectic-like structures formed under high undercooling conditions may arise not only from solid–liquid growth processes, but also from subsequent solid-state decomposition. When combined with our previous study on anomalous eutectic formation under low undercooling conditions [9], the present results suggest that remelting or fragmentation mechanisms are not required to account for the anomalous eutectic morphologies observed in the Ag–Cu system under the conditions studied.

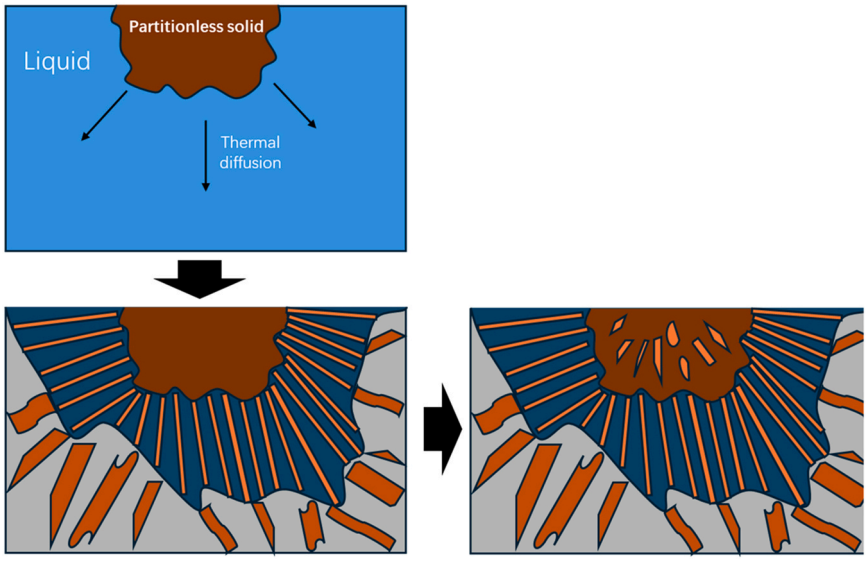

Fig. 13. A schematic of the solidification sequence, showing initial radial outward growth of the partitionless solid, nucleation and further radial outward growth of the eutectic and finally binodal/spinodal decomposition of the partitionless solid.

CRediT authorship contribution statement

Liam S.E. Teggin: Investigation, Formal analysis. **Tiantian Chai:** Visualization, Resources, Methodology, Investigation, Formal analysis. **Robert F Cochrane:** Supervision, Investigation, Formal analysis. **Andrew M Mullis:** Writing – review & editing, Supervision, Software, Methodology, Investigation, Formal analysis, Conceptualization. **Stuart Micklethwaite:** Data curation. **Zabeada Aslam:** Investigation, Data curation. **Huamao Rao:** Writing – original draft, Visualization, Validation, Software, Resources, Methodology, Investigation, Formal analysis, Data curation, Conceptualization.

Declaration of Competing Interest

The authors declare that they have no known competing financial interests or personal relationships that could have appeared to influence the work reported in this paper.

Appendix A. Supporting information

Supplementary data associated with this article can be found in the online version at doi:10.1016/j.jallcom.2026.188306.

References

[1] J.F. Li, W.Q. Jie, S. Zhao, Y.H. Zhou, Metall. Mater. Trans. A Phys. Metall. Mater. Sci. 38 (2007).
[2] T.Z. Kattamis, M.C. Flemings, Metall. Mater. Trans. 1 (1970).
[3] S. Zhao, J.F. Li, L. Liu, Y.H. Zhou, Mater. Charact. 60 (2009).
[4] N. Wang, C.D. Cao, B. Wei, Solidification behaviour of silver-copper alloys in a drop tube, Adv. Space Res. 24 (1999) 1257–1261.
[5] L. Liu, J.F. Li, Y.H. Zhou, Acta Mater. 59 (2011).
[6] R. Goetzinger, M. Barth, D.M. Herlach, Mechanism of formation of the anomalous eutectic structure in rapidly solidified Ni–Si, Co–Sb and Ni–Al–Ti alloys, Acta Mater. 46 (1998) 1647–1655.
[7] B. Wei, D.M. Herlach, F. Sommer, W. Kurz, Mater. Sci. Eng. A (1994) 181–182.
[8] E. Çadirli, D.M. Herlach, T. Volkmann, J. Non Cryst. Solids 356 (2010).
[9] A.M. Mullis, C.R. Clopet, On the origin of anomalous eutectic growth from undercooled melts: Why re-melting is not a plausible explanation, Acta Mater. 145 (2018) 186–195.
[10] C.R. Clopet, R.F. Cochrane, A.M. Mullis, The origin of anomalous eutectic structures in undercooled Ag–Cu alloy, Acta Mater. 61 (2013) 6894–6902.
[11] S. Walder, P.L. Ryder, Critical solidification behavior of undercooled Ag-Cu alloys, J. Appl. Phys. 74 (1993) 6100–6106.
[12] S. Walder, P.L. Ryder, Nonequilibrium solidification in undercooled melts of the alloy Ag-39.9 at. % Cu, J. Appl. Phys. 73 (1993) 1965–1970.
[13] B. Wei, D.M. Herlach, F. Sommer, W. Kurz, Rapid solidification of undercooled eutectic and monotectic alloys, Mater. Sci. Eng. A 173 (1993) 355–359.
[14] B.L. Jones, Metall. Trans. 2 (1971).
[15] L.Q. Xing, D.Q. Zhao, X.C. Chen, Solidification of undercooled Ni-32.5 wt% Sn eutectic alloy, J. Mater. Sci. 28 (1993) 2733–2737.
[16] S.N. Tewari, Metall. Trans. A 18 (1987).
[17] J.F. Li, X.L. Li, L. Liu, S.Y. Lu, Photophysical and photocatalytic properties of Li2M (WO4)2(M = Co and Ni, J. Mater. Res. 23 (2008) 3309–3315.
[18] C. Yang, J. Gao, Y.K. Zhang, M. Kolbe, D.M. Herlach, Acta Mater. 59 (2011).
[19] X. Lin, Y.Q. Cao, Z.T. Wang, J. Cao, L.L. Wang, W.D. Huang, Regular eutectic and anomalous eutectic growth behavior in laser remelting of Ni-30wt%Sn alloys, Acta Mater. 126 (2017) 210–220.
[20] X.X. Wei, X. Lin, W. Xu, Q.S. Huang, M. Ferry, J.F. Li, Y.H. Zhou, Remelting-induced anomalous eutectic formation during solidification of deeply undercooled eutectic alloy melts, Acta Mater. 95 (2015) 44–56.
[21] S. Zhao, J. Li, L. Liu, Y. Zhou, aPCR-SSCP and DNA sequencing detecting two silent SNPs at KAP8.1 gene in the cashmere goat, J. Cryst. Growth 311 (2009) 1387–1391.
[22] S. Azadehranjbar, J.E. Shield, Mater. (Oxf.) 9 (2020).
[23] N. Wang, B.B. Wei, Unified Understanding of Giant Magnetoresistance Effect and Magnetization in Granular Films with Two-Particle Size Distribution, Chin. Phys. Lett. 21 (2004) 2255–2258.
[24] Q.Y. Qin, J.F. Li, L. Yang, L.J. Liu, Solidification behavior and microstructure of Ag–Cu eutectic alloy at different sub-rapid cooling rates, Mater. Chem. Phys. 311 (128521) (2024) 128521.
[25] W. Boettinger, S. Coriell, R. Trivedi, Claitor'S. Publ. Div. Baton Rouge LA (1988) 13–25.
[26] S. Zhang, K. Xiong, R. Yang, H. Dai, H. Wu, J. He, Y. Wang, L. Wu, Y. Mao, Effect of asynchronized and synchronized laser shock peening on microstructure and mechanical properties of the Ti–6Al–4V laser joint, J. Mater. Res. Technol. 26 (2023) 9289–9314.
[27] M.J. Aziz, Model for solute redistribution during rapid solidification, J. Appl. Phys. 53 (1982) 1158–1168.
[28] M.J. Aziz, T. Kaplan, Continuous growth model for interface motion during alloy solidification, Acta Metall. 36 (1988) 2335–2347.
[29] S.L. Sobolev, On the transition from diffusion-limited to kinetic-limited regimes of alloy solidification, Acta Mater. 61 (2013) 7881–7888.
[30] S.L. Sobolev, Effects of local non-equilibrium solute diffusion on rapid solidification of alloys, Phys. Status Solidi A Appl. Res. 156 (1996) 293–303.
[31] S.L. Sobolev, Local-nonequilibrium model for rapid solidification of undercooled melts, Phys. Lett. A 199 (1995) 383–386.
[32] S.L. Sobolev, Local non-equilibrium diffusion model for solute trapping during rapid solidification, Acta Mater. 60 (2012) 2711–2718.
[33] P. Galenko, Solute trapping and diffusionless solidification in a binary system, Phys. Rev. E Stat. Nonlin. Soft Matter Phys. 76 (2007) 031606.
[34] P.K. Galenko, D.A. Danilov, Local nonequilibrium effect on rapid dendritic growth in a binary alloy melt, Phys. Lett. A 235 (1997) 271–280.
[35] J.C. Baker, J.W. Gahn, Solute trapping by rapid solidification, Acta Metall. 17 (1969) 575–578.
[36] K. Eckler, R.F. Cochrane, D.M. Herlach, B. Feuerbacher, M. Jurisch, Evidence for a transition from diffusion-controlled to thermally controlled solidification in metallic alloys, Phys. Rev. B 45 (1992) 5019–5022.
[37] S.N. Ojha, Metastable phase formation during solidification of undercooled melt, Materials Science Engineering A 304–306 (2001) 114–118.

[38] O.V. Gusakov, P.K. Galenko, V.G. Shepelevich, D.V. Alexandrov, M. Rettenmayr, Philos. Trans. R. Soc. A Math. Phys. Eng. Sci. 377 (2019).
[39] A. Manzoni, H. Daoud, R. Völkl, U. Glatzel, N. Wanderka, Phase separation in equiatomic AlCoCrFeNi high-entropy alloy, 212-5, Ultramicroscopy 132 (2013), 212-5.
[40] Y.P. Wang, B.S. Li, M.X. Ren, C. Yang, H.Z. Fu, Mater. Sci. Eng. A 491 (2008).
[41] A. Munitz, L. Meshi, M.J. Kaufman, Mater. Sci. Eng. A 689 (2017).
[42] L.S.E. Teggin, R.F. Cochrane, S.L. Micklethwaite, Z.P. Aslam, A.E. Nassar, A.M. Mullis, Solid-State Decomposition Following Partitionless Solidification in Dendrite Arms of Rapidly Solidified CoCrCuFeNi 0.8 High-Entropy Alloy, n.d.
[43] H. Rao, A. Mullis, R. Cochrane, Eutectic Solidification Morphologies in Rapidly Solidified Hypereutectic Sn–Ag Solder Alloy, Metall. Mater. Trans. A 55 (2024) 4623–4638.
[44] C. Ophus, Four-Dimensional Scanning Transmission Electron Microscopy (4D-STEM): From Scanning Nanodiffraction to Ptychography and Beyond, Microsc. Microanal. 25 (2019) 563–582.
[45] P.R. Subramanian, J.H. Perepezko, The ag-cu (silver-copper) system, J. Phase Equilibria 14 (1993) 62–75.
[46] E.S. Lee, S. Ahn, Acta Metallurgica Et Materialia 42 (1994).
[47] S. Zhao, J. Li, L. Liu, Y. Zhou, J. Cryst. Growth 311 (2009).
[48] M. Erol, U. Boyuk, T. Volkmann, D.M. Herlach, Containerless solidification of Ag–Al and Ag–Cu eutectic alloys in a drop tube, J. Alloy. Compd. 575 (2013) 96–103.
[49] O. Oloyede, T.D. Bigg, R.F. Cochrane, A.M. Mullis, Microstructure evolution and mechanical properties of drop-tube processed, rapidly solidified grey cast iron, Materials Science Engineering A 654 (2016) 143–150.
[50] M. Erol, U. Büyük, Solidification Behavior of Ge–Al Eutectic Alloy in a Drop Tube, Trans. Indian Inst. Met. 69 (2016) 961–970.
[51] G. Shao, P. Tsakiropoulos, Prediction of phase selection in rapid solidification using time dependent nucleation theory, Acta Metall. Et. Mater. 42 (1994) 2937–2942.
[52] J. Lipton, W. Kurz, R. Trivedi, Rapid dendrite growth in undercooled alloys, Acta Metall. 35 (1987) 957–964.
[53] J.F. Li, Y.H. Zhou, Eutectic growth in bulk undercooled melts, Acta Mater. 53 (2005) 2351–2359.
[54] K.A. Jackson, J.D. Hunt, 1988, in: Dynamics of Curved Fronts.
[55] R. Trivedi, P. Magnin, W. Kurz, Theory of eutectic growth under rapid solidification conditions, Acta Metall. 35 (1987) 971–980.
[56] Z. Su, L. Jin-Fu, L. Li, Z. Yao-He, Chin. Phys. B 18 (2009).
[57] H.E. Cline, D. Lee, Strengthening of lamellar vs. equiaxed Ag-Cu eutectic, Acta Metall. 18 (1970) 315–323.
[58] R. Goetzinger, M. Barth, D.M. Herlach, Growth of lamellar eutectic dendrites in undercooled melts, J. Appl. Phys. 84 (1998) 1643–1649.
[59] A.M. Mullis, O.E. Jegede, T.D. Bigg, R.F. Cochrane, Dynamics of core–shell particle formation in drop-tube processed metastable monotectic alloys, Acta Mater. 188 (2020) 591–598.
[60] D.M. Herlaeh, R.F. Cochrane, I. Egry, H.J. Fecht, A.L. Greer, Int. Mater. Rev. 38 (1993).
[61] L.J. Liu, X.X. Wei, M. Ferry, J.F. Li, Investigation of the origin of anomalous eutectic formation by remelting thin-gauge samples of an Ag-Cu eutectic alloy, Scr. Mater. 174 (2020) 72–76.
[62] N. Yan, D.L. Geng, Z.Y. Hong, B. Wei, Formation of ultrafine three-dimensional hierarchical birnessite-type MnO2 nanoflowers for supercapacitor, J. Alloy. Compd. 607 (2014) 245–250.
[63] R.T. Solthin, G.A. Chadwick, Heterogeneous nucleation in solidifying metals, Acta Metall. 26 (1978) 223–231.
[64] J.A. Kittl, M.J. Aziz, D.P. Brunco, M.O. Thompson, Nonequilibrium partitioning during rapid solidification of Si□As alloys, J. Cryst. Growth 148 (1995) 172–182.
[65] J.W. Cahn, ON SPINODAL DECOMPOSITION*, n.d.
[66] M. Tang, A. Karma, Surface modes of coherent spinodal decomposition, Phys. Rev. Lett. 108 (2012) 265701.
[67] O. Pandey, S. Ojha, S. Lele, SPINODAL BOUNDARIES Ag. -Cu Syst. (1993).
[68] T.Le Cheng, Y.H. Wen, NPJ Comput. Mater. 7 (2021).
[69] G.C. Weatherly, Philos. Mag. 17 (1968).
[70] G.C. Weatherly, R.B. Nicholson, Philos. Mag. 17 (1968).
[71] W. Kurz, D.J. Fisher, M. Rappaz, Fundamentals of Solidification 5 Th Fully Revised Edition, n.d.
[72] R. Trivedi, W. Kurz, Dendritic growth, Int. Mater. Rev. 39 (1994) 49–74.
[73] A.M. Mullis, K.I. Dragnevski, R.F. Cochrane, The transition from the dendritic to the seaweed growth morphology during the solidification of deeply undercooled metallic melts, Mater. Sci. Eng. A 375–377 (2004) 157–162.